remote sensing

MDPI

Article

Thermal Energy Release Measurement with Thermal Camera: The Case of La Solfatara Volcano (Italy)

Enrica Marotta [1,*], Rosario Peluso [1,*], Rosario Avino [1], Pasquale Belviso [1], Stefano Caliro [1], Antonio Carandente [1], Giovanni Chiodini [2], Giovanni Macedonio [1], Gala Avvisati [1] and Barbara Marfè [3]

1 Istituto Nazionale di Geofisica e Vulcanologia, Osservatorio Vesuviano, 80124 Napoli, Italy; rosario.avino@ingv.it (R.A.); pasquale.belviso@ingv.it (P.B.); stefano.caliro@ingv.it (S.C.); antonio.carandente@ingv.it (A.C.); giovanni.macedonio@ingv.it (G.M.); gala.avvisati@ingv.it (G.A.)

2 Istituto Nazionale di Geofisica e Vulcanologia, Sezione di Bologna, 40128 Bologna, Italy; giovanni.chiodini@ingv.it

3 Freelance, Napoli 80144, Italy; bimar1982@yahoo.it

* Correspondence: enrica.marotta@ingv.it (E.M.); rosario.peluso@ov.ingv.it (R.P.); Tel.: +39-338-454-67-24 (E.M.); +39-339-746-83-31 (R.P.)

Received: 6 December 2018; Accepted: 15 January 2019; Published: 17 January 2019

Abstract: Quiescent volcanoes dissipate a large part of their thermal energy through hot soils and ground degassing mainly in restricted areas called Diffuse Degassing Structures. La Solfatara crater represents the main spot of thermal release for the Campi Flegrei volcano (Italy) despite its reduced dimensions with regards to the whole caldera. The purpose of this study was to develop a method to measure thermal energy release extrapolating it from the ground surface temperature. We used imaging from thermal cameras at short distances (1 m) to obtain a mapping of areas with thermal anomalies and a measure of their temperatures. We built a conceptual model of the energy release from the ground to atmosphere, which well fits the experimental data taken in the La Solfatara crater. Using our model and data, we could estimate the average heat flux in a portion of the crater as $q_{avg} = 220 \pm 40\,W/m^2$, compatible with other measurements in literature.

Keywords: thermal flux measurement; IR camera; La Solfatara volcano

1. Introduction

One of the most obvious signals of activity of a volcano is the fumarolic emission and the associated heat release [1,2]. Often, the steam is not emitted by the fumaroles but condenses in the subsoil forming hot soils diffusely degassing the incondensable species (mainly CO_2). Hot soils and ground degassing does not occur throughout the whole volcanic or hydrothermal areas, but from restricted areas called Diffuse Degassing Structures (DDS), commonly associated with areas of high permeability related to faults or fractures [3,4]. It is worth noting that the thermal energy emitted by DDSs may represent one of the largest terms of the energy balance of quiescent volcanoes [3–9] as demonstrated, for example, at Campi Flegrei caldera (south of Italy), where the thermal emission of La Solfatara DDS (~1 km^2, Figure 1) is of primary importance in the energetic balance of the caldera. Geothermal fluids at La Solfatara are rich in H_2O, which condensates at few cm under the soil releasing heat that is then mainly transported to the surface in a conductive regime. We emphasize that the thermal energy released by the hot soils of La Solfatara (~10^{13} J/d [3]) is much larger than both the heat conductively transmitted over the entire caldera (~100 km^2) and the energy dissipated by earthquakes and ground deformation [3] in the current period of volcanic quiescence.

Currently, the heat flux from hot soils is estimated with time consuming measurement campaigns of either shallow thermal gradients [10] or CO_2 fluxes [3].

Estimates of the heat flux based on measurements of the thermal gradient has been used on several volcanoes, including Mount Hood [11], Mount Rainier [12], Etna [13], Campi Flegrei [4] and Vulcano [14]. In particular, Chiodini et al. [4] estimated a soil thermal conductivity between 0.4 and 2.3 $W\,m^{-1}\,K^{-1}$ at La Solfatara.

In this frame, the specific objective of the work was to test a methodology based on infrared (IR) images that, thanks to recent technology advancements, potentially can be used for quick, safe and cheap measurements of large areas and/or of inaccessible sites.

Thermal cameras have already been widely used in the case of lava flows (e.g., [15,16]), and fumarolic zones [17–21]. Gaudin et al. [22] at La Soufrière proposed a method to estimate ground heat flux from surface thermal anomalies in zone with medium/low flux (<500 W/m^2) where steam mainly condensates in the soil close to the surface, conditions similar to those of La Solfatara volcano, where Chiodidni et al. [3] estimated a flux of ~200 W/m^2.

Our work regards the measurement of this important portion of energy emitted by the hydrothermal sites of volcanoes and geothermal areas. The study of this heat flux: (i) may give a fundamental contribution to the knowledge of the dynamics of a volcanic systems [4,23,24]; (ii) may constitute a powerful tool for the monitoring of volcanic activity [25–28]; and (iii) could potentially constitute a cheap way to estimate the geothermal potential of hydrothermal sites.

2. Study Area

The La Solfatara crater (4200 calibrated (cal.) year B.P. [29]) is located at 100 m above sea level, in the central part of Campi Flegrei caldera (CFc), in the south of Italy (Figure 1).

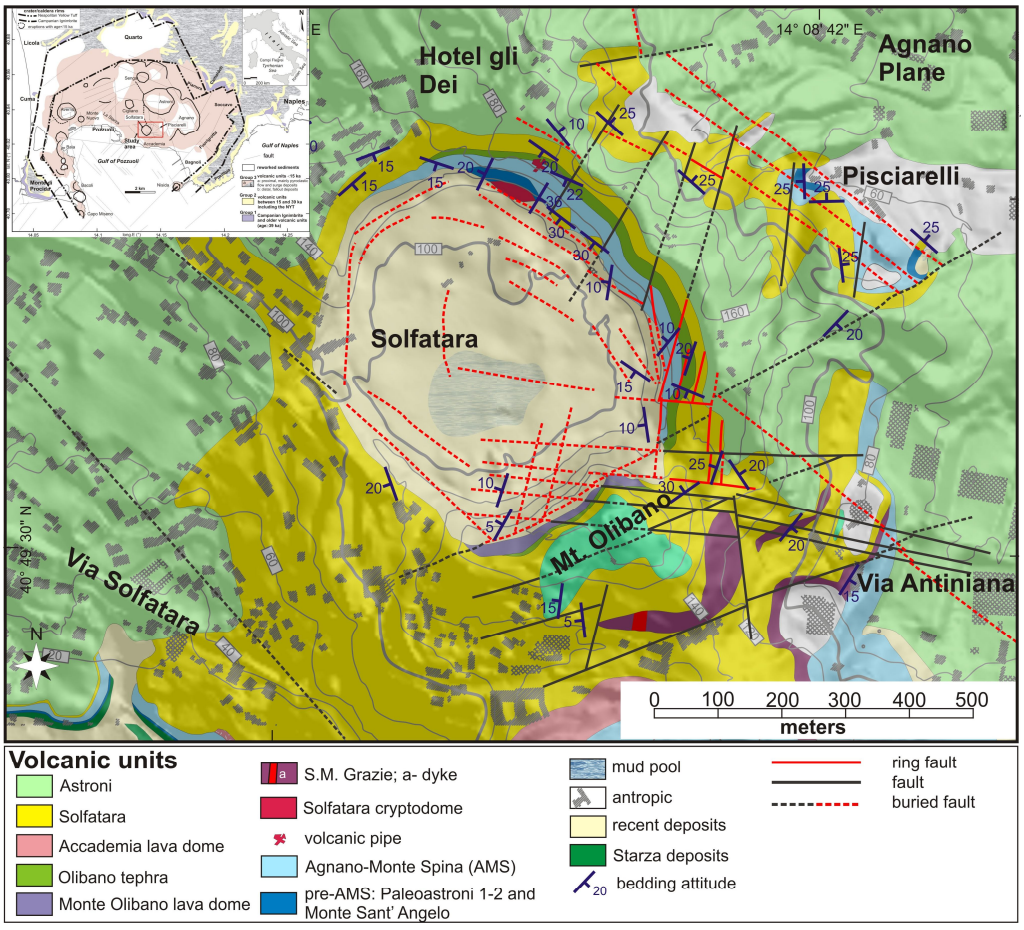

Figure 1. Structural/geological map of La Solfatara crater after Isaia et al. [29].

The crater is a 0.5×0.6 km sub-rectangular structure, whose geometry is mainly due to the control exerted by N40-50W and N50E trending fault systems, which crosscut the area and have been active many times during the main volcano-tectonic events that affected the Campi Flegrei caldera (CFc). The fumarolic activity is mainly concentrated in the southeastern part of the crater at the intersection between the NW and the NE trending fractures. The central part of La Solfatara crater is occupied by a mud pool, in which the water-table emerges and a continuous rising of hydrothermal fluids generates diffuse bubbling. Most of the crater is affected by anomalous soil diffuse degassing of CO_2 [3] that also extends outside the crater. In the period 1998–2016, the total amount of hydrothermal CO_2 diffusively emitted by La Solfatara DDS varied from ~1000 to ~2000 ton/day [30]. Soil temperature distribution also shows the direct control exerted by the structures on the heat flux [31].

La Solfatara is the most active site of the CFc whose central part is characterized by a resurgent phenomenon, causing the uplift of differentially displaced blocks, the most uplifted of which (La Starza marine terrace) raised up about 90 m in the past 10 ky [32]. Ground uplift and subsidence events of the caldera floor, known as bradyseism (see, e.g., [32,33]), occurred repeatedly up today with a maximum deformation area located around the town of Pozzuoli near La Solfatara. Different approaches aimed at reconstructing the processes governing the recent caldera dynamics, have revealed that these unrest episodes were related to a complex interaction with the deep magmatic source and the shallow hydrothermal system [29,34].

Geophysical and hydro-geological investigations at La Solfatara volcano [35–37] provide images of the shallow and intermediate subsurface of the crater. These authors, using electromagnetic and electrical data, recognized two main electrical zones: an outcropping resistive layer (A) overlying a conductive one (B). Layer A represents a clayey, non-saturated zone, and Layer B corresponds to a hydrothermal aquifer recharged through condensation of geothermal fluids.

At a deeper level, evidences of gas or fluid reservoir beneath La Solfatara area come from the recent seismic attenuation imaging of Campi Flegrei by De Siena et al. [38] who recognized vertically extending, high attenuation structures. This result is compatible with that of Battaglia et al. [39] who observed a high V_p/V_s anomaly in the southwestern part of La Solfatara, as expected for a strongly fractured medium permeated by fluids.

3. Materials and Methods

In this work, we tested the possibility of using thermal images of the ground as a proxy for the conductive thermal flux from the hot soil of DDSs to the surface. We performed two sets of measurements: (1) soil temperatures by IR camera; and (2) temperature gradients in the soil. Then, the estimates of heat flux based on the thermal gradient were compared with the estimates based on the soil temperatures acquired with the IR camera at the same time.

3.1. Materials

3.1.1. Measurement of the Soil Temperature by IR Camera

We performed many campaigns in the La Solfatara crater measuring the surface temperature, the air temperature and relative humidity. These measurements were used to estimate the thermal flux from the soil. Moreover, we measured the shallow temperature gradient in the first few tens of cm of soil to obtain an independent estimate of the conductive thermal flux (see Section 3.1.2). Campaigns were done over a time span of several years (2011–2017) and during different seasons to understand any eventual dependence on weather conditions and to assess the stability of soil conditions over time. A map of the sampled points (352 points, including the background point, "BG") is reported in Figure 2. We performed the measures in non-vegetated areas of the crater and neglecting the effects of soil roughness.

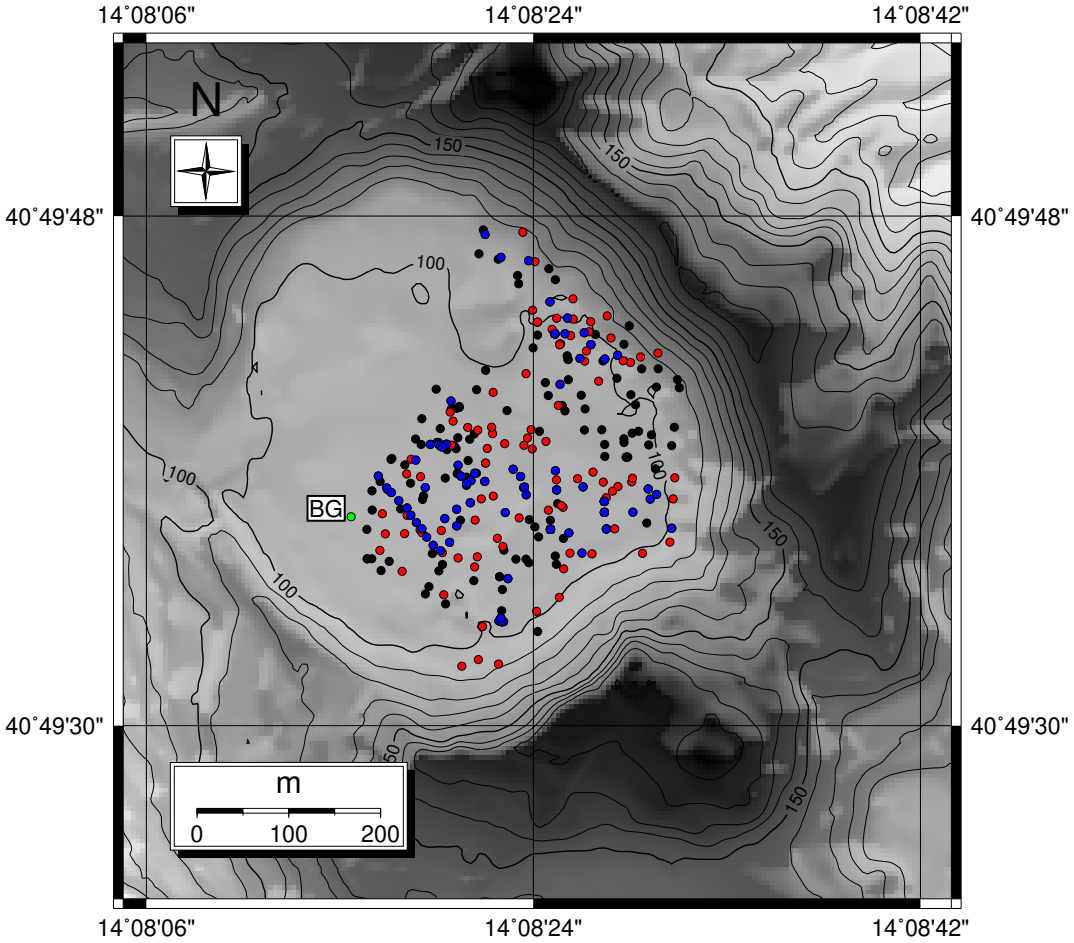

Figure 2. Map of the sampled points at La Solfatara volcano (Campi Flegrei) in the period 2011–2017. The total number of point is 352, including the background point (green point, BG): black points are the points with an inverted gradient (Figure 3c), red points are those with a direct one (Figure 3a,b,d), among which we selected those only acquired during night (blue points), see also Section 3.1.2. The northwestern part of the crater surface has not been sampled as it is highly vegetated.

The campaigns can be roughly divided into two separate phases: in the first one, we moved randomly over the whole area of the crater trying to cover as much as possible of its surface. In the second one, we performed systematic, grid spaced surveys.

For each point, we measured the surface temperature by means of a handheld thermal camera FLIR SC640 kept at about 1 m over the soil using a tripod and shallow gradients using a graduated thermocouple inserted at various depths into the ground (for details on the usage of FLIR SC640 thermal camera, see, e.g., Marotta et al. [40]; a summary of its technical characteristics is reported in Table 1). Surface thermal images were taken just before the insertion of the thermocouple to avoid perturbations to the shallow thermal system due to the presence of the thermocouple itself.

Table 1. Main characteristics of the thermal camera.

Model	**FLIR SC640**
Detector Type	Uncooled Microbolometer, FPA (Focal Plane Array)
Resolution	640 × 480 pixel
Spectral range	7.5 ÷ 13 µm
Precision	±2 °C or ±2% of reading
Thermal sensitivity	<0.06 °C at +30 °C
Focal length	37.64 mm
Spatial resolution	0.66 mrad

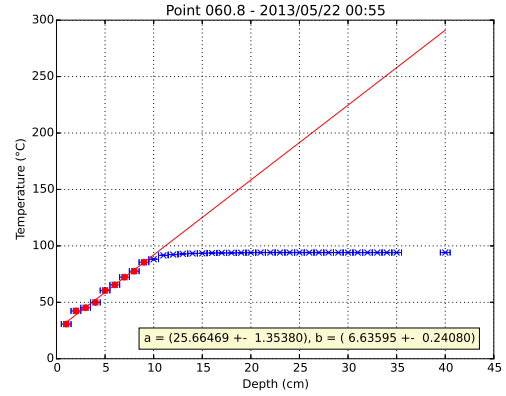

(**a**)

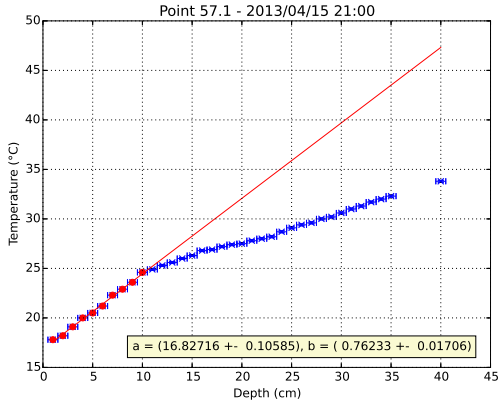

(**b**)

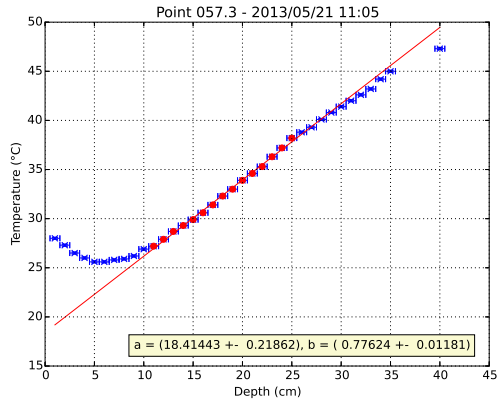

(**c**)

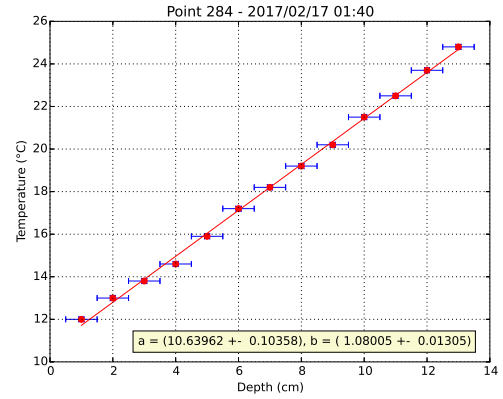

(**d**)

Figure 3. Temperature profile examples: (**a**) saturated profile; (**b**) slope changing gradient; (**c**) inverted gradient; and (**d**) fully linear. Points of type: (**a**,**b**,**d**) are the red and blue ones of Figure 2; and (**c**) are the black ones in the same figure. The yellow box of each sub-figure is the result of the linear fit performed on the red points in the form $T = a + bz$ being T the measured temperature and z the depth.

For each campaign, we selected some points characterized by a negligible heat flux to determine a background level for both the surface temperature and shallow gradients, assuming that the surface temperature measured in these points was only affected by external factors. The background value for the surface temperature was used to estimate the radiation temperature of the sky needed to correct the radiative heat flux. Once we were confident that a particular point was stable enough over time, we only used it as the background (green point labeled "BG" in Figure 2).

Surface temperatures, gradients and the state of the surface hydrothermal system are affected by meteorological conditions: solar radiation, atmospheric pressure, wind and rain change the way heat is transported to the surface and from the surface to the atmosphere (e.g., [41,42]). Two of the campaigns were committed to study the influence of solar irradiation on shallow gradients by measuring them for 24 h at a small number of points. These campaigns took place between spring and summer to avoid heavy rain that may have influenced temperatures and gradients [42–44].

External conditions also influence the way that the thermal camera returns the acquired data. Atmospheric temperature and relative humidity were always measured during IR acquisitions using a TERSID HD2101 thermo-hygrometer and input into the internal software of the camera to correct for their influence. Following Gaudin et al. [22], we neglected the effects of the wind on thermal images as the short shooting distances does not affect the measurement. To take into account some marginal micro-climatic effect, for each point, we shot several thermal images taking the mean temperature and standard deviation of the images and using their weighted average as the point surface temperature. The same procedure was also used at the background point BG. Measures at the background point BG were repeated several times during each campaign to obtain a trend of its values in time. Following Flynn et al. [45] and Pinkerton et al. [46], we used the value of 0.98 for the relative emissivity, as also reported in Table 2.

Table 2. Parameters and results.

Description	Symbol	Value	Unit
Typical parameters (evaluated at 30 °C)			
Atmospheric pressure (assumed constant)	P_{air}	1.01325×10^5	Pa
Diffusion coefficient of vapor in air	D_{va}	2.58×10^{-5}	m^2/s
Lewis number	Le	0.857	—
Kinematic viscosity of the air	ν	1.35×10^{-5}	m^2/s
Molecular weight of air	M_a	0.029	kg/mol
Molecular weight of water	M_w	0.018	kg/mol
Relative emissivity of the surface	ε_r	0.98	—
Specific heat of air at constant pressure	c_{pa}	1004.67	J/kg K
Stefan-Boltzmann constant	σ	5.67×10^{-8}	$W/m^2\,K^4$
Thermal conductivity of the air	k_{air}	0.026	W/mK
Thermal expansion coefficient of the air	β	3.69×10^{-3}	1/K
Thermal diffusivity of the air	α	2.21×10^{-5}	m^2/s
Results from best fits and estimates.			
Thermal conductivity of the soil	k_{soil}	0.88 ± 0.07	$W/(K \cdot m)$
Total power released through the investigated surface	Q_{tot}	22 ± 4	MW
Average heat flux on the investigated surface	q_{avg}	220 ± 40	W/m^2

In the present work, we avoided the use of the thermal camera in windy conditions or sun irradiation, and we selected only measurements performed at night or in the first hours of the day just before sunrise (from 22:00 to 7:00 local time). Since during the measurements, the soil of La Solfatara was always wet, we considered the effect of soil evaporation in the thermal balance at the surface (see Section 3.2).

3.1.2. Measurement of the Temperature Gradient of the Soil

Measurements of the shallow temperature profile at La Solfatara were performed in conjunction with the measurements of the surface temperature by the IR camera and in the same points, as reported in Figure 2.

Temperatures were measured by using a graduated K-type thermocouple inserted into the ground in the first few tens of cm with steps of 1 cm. The observed gradients may be classified in a few different types [22]. High flux zones are characterized by a buffer zone few centimeter under the soil (Figure 3a) where the temperature is quite stable due to the condensation of H_2O vapor and then it has a rapid quite-linear decrease up to the surface. Medium flux areas may show a change in the trend of the vertical profiles where the heat transport pass from a mixed (conductive/advective) regime to a pure conductive regime (Figure 3b). Low flux points (Figure 3c) are often characterized by gradients quite linear on the whole profile and are the ones that are mostly influenced by external temperature conditions, sometimes showing an inverse gradient at the shallowest part. For this reason, they were discarded for the purposes of this work. In the other three cases, we calculated the gradients via a linear fit of the topmost part of the profile (Figure 3a,b,d).

To double check the measured surface temperatures with the fitted gradients, for each nightly point, we report in Figure 4 the comparison between the surface temperature measured via IR camera and the extrapolation at zero depth of the gradient.

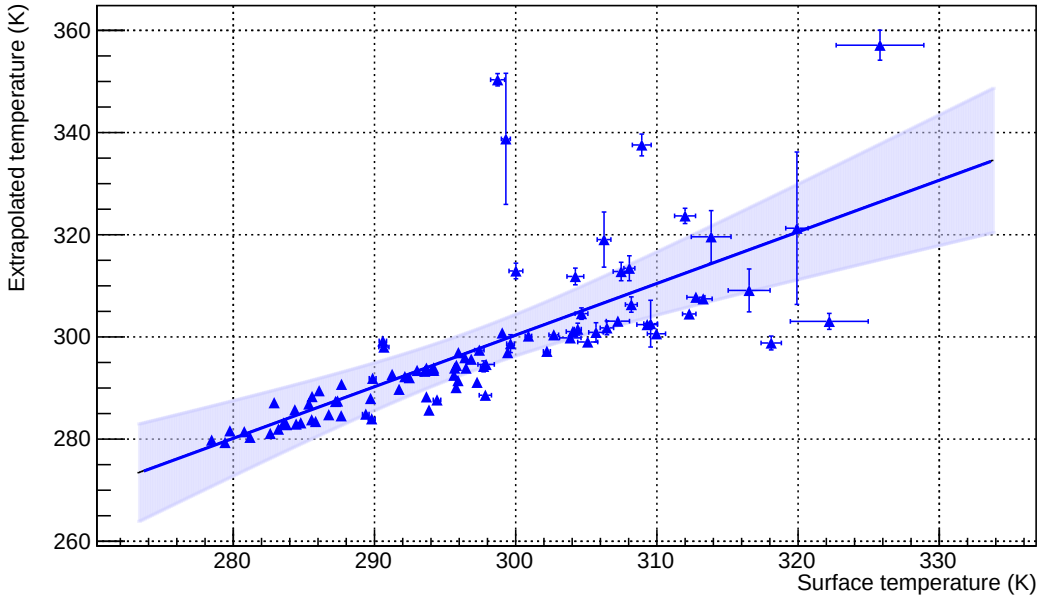

Figure 4. Comparison between surface temperatures, measured with IR camera (abscissa) and extrapolation of gradients at zero depth (ordinate) for each nightly point. The line represents the best fit of the dataset with a linear model. Results of the fit give values of -3 ± 30 K for the intercept and 1.01 ± 0.10 for the angular coefficient; the correlation factor is about 0.8 over 91 points. The light blue band represents fit limit at 95% Confidence Level (CL).

Figure 5a shows the result of a 24 h campaign in one of the points picked out for background measurement, where heat flux coming from below was basically null. As hours go by, the thermal wave due to solar irradiation penetrated the ground and its wavelength could be evaluated. Instead, Figure 5b shows the effect due to solar irradiation in a point where heat flux was not negligible. It can be observed how, in the warmest hours of the day, the gradient reversed, telling us that the best time to measure temperatures is at dawn just before sunrise. A similar effect is to be expected during the year, but it is related to seasonal temperature changes: a continuous monitoring of external temperatures and thermal gradient is then necessary. To avoid the effect of sun irradiation as much as possible,

we decided to use for the purposes of this work only gradients of Types (a), (b) and (d) (Figure 3) sampled during night hours (22:00 to 07:00 local time). These points are the ones marked in blue in Figure 2. Results for the whole sampling set are reported in the Supplementary Materials.

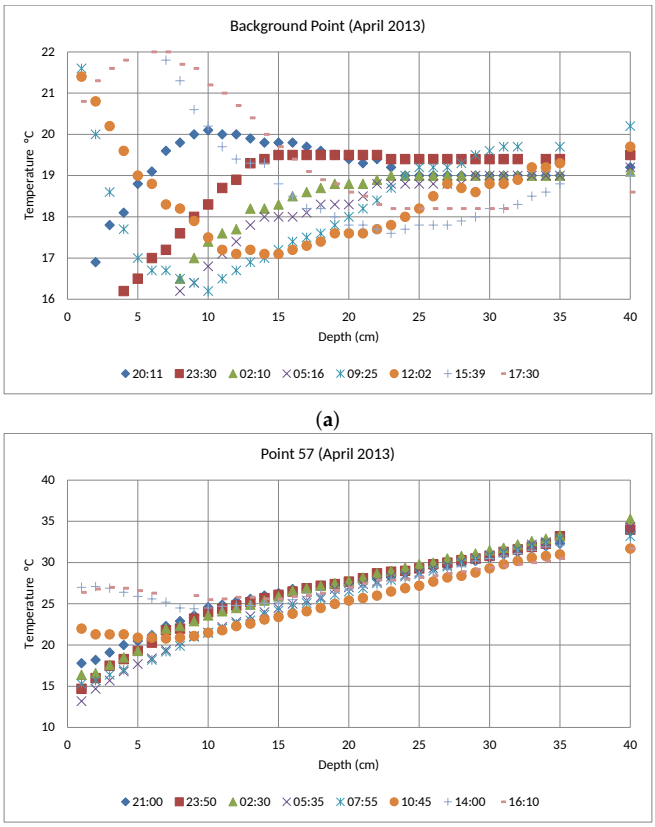

Figure 5. Results of thermal profile measurements on a 24 h campaign: in a background point (BG) (**a**); and in a point with a small thermal flux (**b**). At the bottom of the boxes, there are the hours of acquisition of each profile.

Since this method only gives punctual measurements of the thermal gradient, it is a very time consuming methodology when used to estimate the heat release from a large area, because it needs the collection of several samples and it may require weeks to be brought to a conclusion [13,14,47].

3.2. Methods

Under the steady state condition, the conductive thermal flux from the hot soil of the DDSs to the surface (q_{soil}) equals the sum of the radiative flux (q_{rad}), the convective flux from the surface to the atmosphere (q_{conv}) and the heat needed for the evaporation of the water from the surface of the wet soil (q_{evap}). These variables can be roughly estimated with IR images and measurements of the atmospheric temperature and humidity. We write the energy balance as:

$$q_{soil} = q_{rad} + q_{conv} + q_{evap} \tag{1}$$

Near the surface, the conductive flux follows the Fourier's law:

$$q_{soil} = -k_{soil} \left(\frac{\mathrm{d}T_{soil}}{\mathrm{d}z} \right) \Big|_{z=0} \tag{2}$$

with k_{soil} and T_{soil}, respectively, being thermal conductivity and temperature of the soil.

The radiative heat transfer follows the Stefan–Boltzmann law, and is parameterized as:

$$q_{rad} = \varepsilon_r \sigma \left(T_s^4 - T_{sky}^4 \right) \tag{3}$$

where ε_r is the relative emissivity of the soil, σ is the Stefan–Boltzmann constant, T_s is the temperature of the soil surface and T_{sky} is the radiation temperature of the sky.

The convective heat transfer from the surface to the atmosphere, in absence of wind, is parameterized as:

$$q_{conv} = h_{conv} \left(T_s - T_{air} \right) \tag{4}$$

where h_{conv} is the convective heat transfer coefficient and T_{air} is the air temperature. The coefficient h_{conv} is typically obtained from the Nusselt number, which is considered a function of the Rayleigh number:

$$Nu_L = \frac{h_{conv} L}{k_{air}} = c \, Ra_L^n \tag{5}$$

where Nu_L and Ra_L are the Nusselt and Rayleigh numbers relative to a heated surface of length scale L, and c and n are empirical constants. The Rayleigh number is defined as:

$$Ra_L = \frac{g\beta \left(T_s - T_{air} \right) L^3}{\nu\alpha} \tag{6}$$

where g, β, ν and α are, respectively, the gravity constant, thermal expansion coefficient, kinematic viscosity and thermal diffusivity of the air.

For square horizontal surfaces of side L, located below a fluid, the empirical coefficients c and n of Equation (5) were determined experimentally by Al-Arabi and El-Riedy [48], as also reported by Incropera and DeWitt [49].

For $T_s > T_{air}$:

$$Nu_L = 0.54 \, Ra_L^{1/4} \qquad \text{for} \quad 10^4 \leq Ra_L \leq 10^7 \tag{7}$$

$$Nu_L = 0.15 \, Ra_L^{1/3} \qquad \text{for} \quad 10^7 \leq Ra_L \leq 10^{10} \tag{8}$$

For $T_s < T_{air}$:

$$Nu_L = 0.27 \, Ra_L^{1/4} \qquad \text{for} \quad 10^5 \leq Ra_L \leq 10^{10} \tag{9}$$

We observed that, when the surface is hotter than the fluid and the Rayleigh number is greater than 10^7 (i.e., in most of our situations), the Nusselt number (Equation (8)) is independent of the length scale L.

In the case of wet soil, part of the heat is needed for evaporation of the water. The corresponding heat flux is parameterized as:

$$q_{evap} = \dot{m}_w L_{lv} \tag{10}$$

where $\dot{m}_w$ is the mass flux of the evaporating water (kg/m^{2}s) and L_{lv} is the latent heat of the water–vapor transition (J/kg).

We considered that the flux of vapor near the soil is controlled by the density gradient of the vapor:

$$\dot{m}_w = h_m (\rho_{vs} - \rho_{va}) \tag{11}$$

where ρ_{vs} and ρ_{va} are, respectively, the densities of the vapor near the soil and in the air, and h_m is the mass transfer coefficient for the vapor in the atmosphere. The density of the vapor at the soil is evaluated at temperature T_s and saturation pressure $p_{sat}(T_s)$, whereas the density of the vapor in

the atmosphere is evaluated at temperature T_a and saturation pressure $p_{sat}(T_a)$ multiplied by the (measured) relative humidity R_w. We assumed perfect gas:

$$\rho_{vs} = \frac{p_{sat}(T_s)M_w}{\mathcal{R}T_s} \quad (12)$$

$$\rho_{va} = R_w \frac{p_{sat}(T_a)M_w}{\mathcal{R}T_a} \quad (13)$$

where $\mathcal{R}$ is the universal constant of gas and M_w is the molecular weight of the water (see Table 2). The saturation pressure of the vapor in the atmosphere was evaluated following Jacobson [50]:

$$p_{sat}(T) = 611.22 \times \exp\left[17.67 \times (T - 273.16)/(T - 29.65)\right] \quad (14)$$

with p_{sat} the saturation pressure in Pa and T the temperature in Kelvin.

The mass transfer coefficient for the vapor in the atmosphere h_m is estimated according to the mass–energy transport analogy [49], i.e.,

$$h_m = \frac{h_{conv}}{\rho_a c_{pa} Le^{1-n_m}} \quad (15)$$

where ρ_a is the air density, c_{pa} is the specific heat of air at constant pressure, Le is the Lewis number and n_m is a coefficient (according to Incropera and DeWitt [49], we assumed $n_m = 1/3$). The Lewis number Le is the ratio between the thermal diffusivity of the air α and the diffusion coefficient of the vapor in the air D_{va}:

$$Le = \frac{\alpha}{D_{va}} \quad (16)$$

The air density ρ_a in Equation (15) was evaluated, assuming a perfect gas, at atmospheric pressure P_{air} and mean temperature between soil and air: $T_{mean} = (T_s + T_a)/2$.

$$\rho_a = \frac{P_{air}M_a}{\mathcal{R}T_{mean}} \quad (17)$$

with M_a the molecular weight of air (see Table 2).

Finally, we estimated the radiation temperature of the sky from the heat balance at a surface where the conductive flux from the soil can be neglected (the background point BG). This condition can be written as:

$$q^b_{rad} + q^b_{conv} + q^b_{evap} = 0 \quad (18)$$

where the superscript ^{b} indicates that the fluxes refer to the background point BG. By using Equations (3) and (4), we obtained the effective radiative temperature of the sky from the soil and air temperatures:

$$T^4_{sky} = T^4_b - \frac{q^b_{conv} + q^b_{evap}}{\varepsilon_r \sigma} \quad (19)$$

where T_b is the temperature of the soil in the background point BG. Fluxes q^b_{conv} and q^b_{evap} are functions of T_b, T_{air} and air humidity R_w, and were evaluated as above with T_s replaced by T_b.

Parameters β, ν, α, c_{pa}, D_{va}, k_{air}, and Le depend on temperature and pressure. In Table 2, we report typical values evaluated at T = 30 °C and P = 1.01325×10^5 Pa (1 atm).

3.2.1. Summary of the Procedure

To evaluate the thermal flux from the soil based on IR and air temperature data, we used the following procedure:

1. Measure T_s by IR camera

2. Measure the temperature T_b at the background point BG by IR camera
3. Measure the air temperature T_{air} (thermometer)
4. Measure the air relative humidity R_w
5. Evaluate the Rayleigh number (Equation (6)), estimate the convective heat transfer coefficient h from the Nusselt number (Equation (5)), and evaluate the convective flux q_{conv} (Equation (4))
6. Estimate the mass transfer coefficient for the evaporation flux h_{evap} (Equation (15)) and evaluate the evaporation heat flux (Equations (10)–(13))
7. Estimate q^b_{conv} and q^b_{evap} at background and evaluate T_{sky} (Equation (19))
8. Estimate the radiative flux (Equation (3))
9. Evaluate the total flux: $q_{soil} = q_{rad} + q_{conv} + q_{evap}$

In the present work, we also obtained an independent estimate of the thermal flux by measuring the thermal gradient in the soil q_{soil}. A best fit was performed, on a linear model in the form:

$$q_{soil} = a + k_{soil} \nabla T_s \tag{20}$$

to obtain the thermal conductivity of the soil k_{soil}, which resulted in agreement with the measurements of Chiodini et al. [4]. The results of this fit are shown in Figure 6.

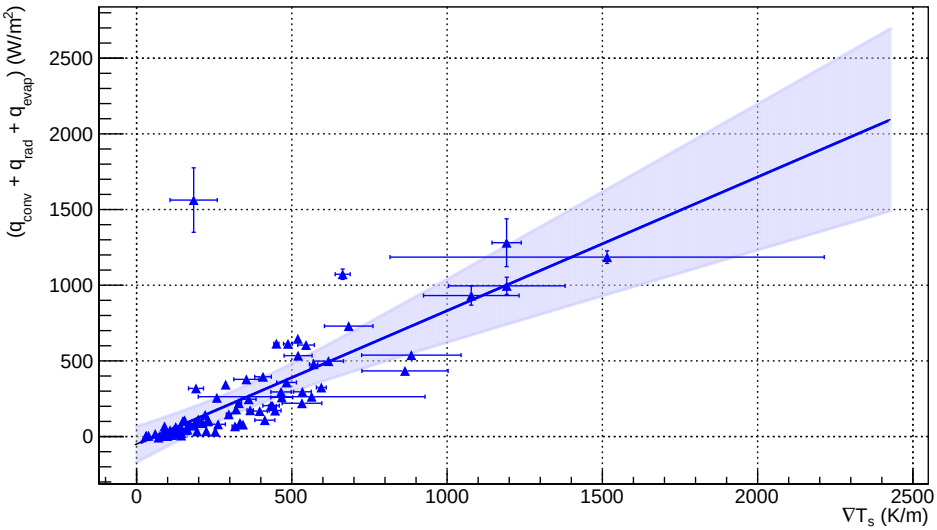

Figure 6. Plot of the total heat flux from the soil (convective, radiative and due to water evaporation), estimated from the measurement of the soil temperature, air temperature and humidity vs. the measured temperature gradient in the soil (∇T_s). To avoid the effect of sun radiation, only measurements performed between 22:00 and 7:00 (local time) were selected. The line represents the best fit of q_{soil} with a linear model: the angular coefficient is the thermal conductivity of the soil k_{soil}. Results of the fit give a value of -50 ± 30 W/m^2 for the a parameter in Equation (20) (congruent with 0 at 95% CL) and $k_{soil} = 0.88 \pm 0.07$ W / (K·m). Light blue band is the fit limits at 95% CL.

4. Results

In the period 2011–2017, we acquired at La Solfatara (Figure 1) temperature profiles of the soil in the first tens of cm, air temperature, air humidity and soil temperature by IR images. To avoid the influence of the sun radiation, the measurements were performed during the night (between 22:00 and 7:00 local time) when we assumed a steady state condition for the heat exchange between soil and air. This condition was also verified by the linearity of the temperature profiles.

For what concerns the radiative heat transfer, we obtained the effective radiative temperature of the sky from the temperatures of the background points and air. The background points are characterized by negligible thermal gradient.

The proposed method allowed estimating the heat flux from the soil from measurements performed above the soil. To verify the method, we plotted the sum of the convective, radiative and evaporation fluxes measured/estimated outside the soil against the conductive flux in the soil obtained from the measurements of the temperature gradient in the soil. For the conversion between the temperature gradient and the thermal flux (see Equation (2)), we performed a fit for the best thermal conductivity of the soil k_{soil}. A value of $k_{soil} = 0.88 \pm 0.07\,\mathrm{W\,m^{-1}K^{-1}}$ was obtained, in accordance with the measurements of thermal conductivity previously performed at La Solfatara by Chiodini et al. [4] who found values between 0.4 and 2.3 $\mathrm{W\,m^{-1}\,K^{-1}}$.

The result is shown in Figure 6, where the sum of the radiative, convective and evaporation thermal fluxes, estimated from measurements performed above the soil are compared with the vertical thermal gradient of the ground.

Using the proposed procedure (Section 3.2.1), we computed the heat flux over the investigated area during the field campaigns. For this purpose, we computed for each measurement point $q_{rad} + q_{conv} + q_{evap}$ of Equation (1) only on points acquired between 22:00 and 07:00 local time (blue points of Figure 2). As these points are discretely distributed on the Solfatara crater area, we elaborated the data with the geostatistical approach proposed by Cardellini et al. [51] used there to produce maps of the CO_2 flux. This method is based on sequential Gaussian simulations (sGs) that consist of the production of numerous equiprobable realizations of the spatial distribution of an attribute (i.e., maps of heat flux in this study), here performed using the SGSIM algorithm of the GSLIB software library [52]. We show the result of this calculation in Figure 7: integrating over the whole investigated area, we estimated a power release $Q_{tot} = 22 \pm 4\,\mathrm{MW}$ on the surface and an average heat flux of about $q_{avg} = 220 \pm 40\,\mathrm{W/m^2}$, in accordance with Chiodini et al. [3].

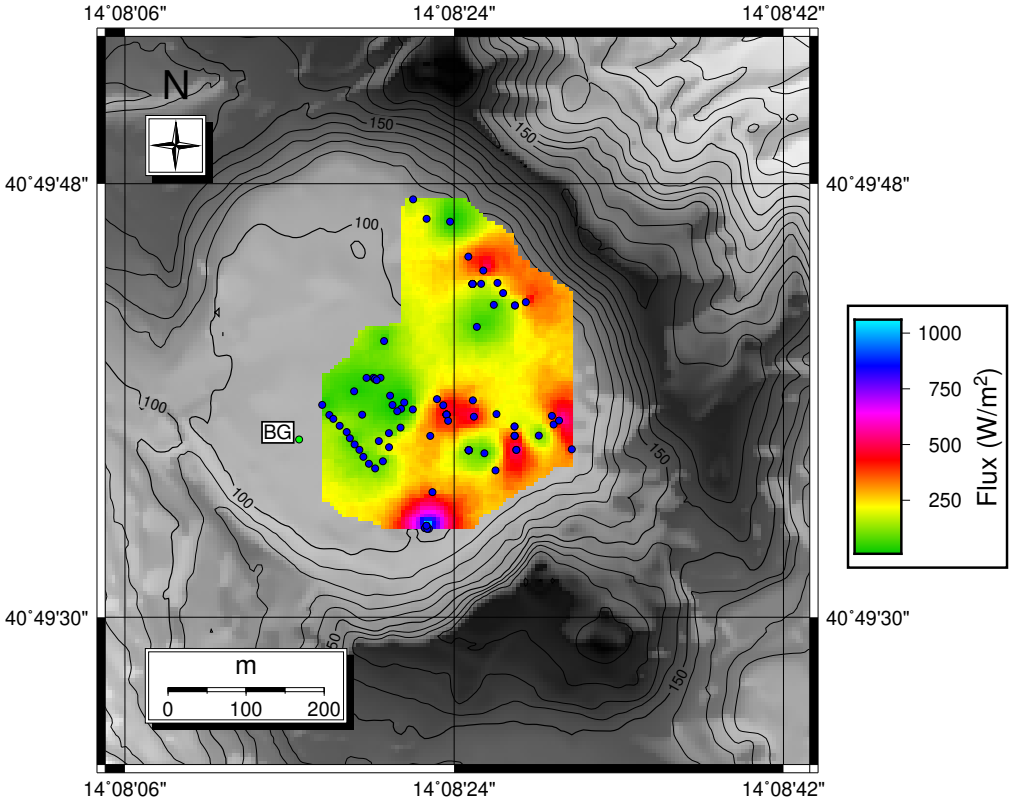

Figure 7. Map of the calculated heat flux distribution over the investigated area using points sampled during nights (blue dots). The green dot represents the background point (BG) site.

In the Supplementary Materials, we also show the same results calculated over the whole set of measurement points (red and blue points together in Figure 2, which are all points of Types (a), (b)

and (d) in Figure 3) as here we discarded points sampled during daytime to avoid the effect of sun irradiation (see Section 3.1.2).

5. Discussion

Volcanoes release large amounts of energy through the transfer of heat from the hot soils of hydrothermal sites to the atmosphere. Up to now, this flux of energy has been measured with time consuming techniques that, e.g., cannot be safely applied in dangerous situations such as at volcanoes in eruption or approaching eruptions. In addition, for this reason, detailed and systematic monitoring data series of the heat flux from volcanic hot soils currently do not exists. Our aim was to explore the possibility to measure this heat flux based on IR images. The experiment consisted in the repetition of numerous combined night measurements of surface temperature by IR camera and temperature gradients. The results are positive because we demonstrated how nighttime thermal images can be used to estimate the total thermal release. In particular, applying soil and atmosphere heat transfer models, we show that the superficial temperatures are those expected for wet soils characterized by thermal gradients close to the measured values and by typical thermal conductivities.

Classical methods to estimate the energy release (CO_2 flux and thermal gradients measurements) do not provide synoptic view of heat flow as they only give punctual measurements. Using the proposed method, it is possible to use IR camera surveys to provide fast and areal estimates of the energy released on areas affected by thermal anomalies. Infrared cameras operate at wavelengths with a low sensitivity to water vapor [53], which is often the main fumaroles gas. Moreover, as the measurement distance increases, so does the pixel size and the absorbance or scattering of radiation along the path between the fumaroles and the sensor. Large pixels include both hot fumaroles regions and cool, surrounding rocks, thus reporting a lower temperature [54]. Scattering or absorbance of radiation along the path depends on atmospheric conditions and is therefore affected by weather conditions. These considerations tells us that the use of long range (kilometer to hundreds of kilometer) thermal cameras may be affected by great errors. These also includes remote sensing through the use of satellite thermal images, which are greatly affected by the infrequent nature of their passes and the needing of cloud-free conditions [20].

The method suits well performing thermal surveys at short/medium distances using drone-borne thermal cameras. A Remotely Piloted Aircraft System (RPAS) can fly from few tens to some hundreds of meters from the soil acquiring thermal images of the surface with a nice resolution and affected by atmospheric induced errors smaller than those, for example, of satellite images. The use of RPAS can also address for the needs of safety of operators and the possibility to map otherwise inaccessible areas. Single thermal shots can be glued together in order to obtain a global thermal map of the investigated area and, once converted to energy release, can give both areal information of the global thermal release and detailed estimates of the conductive energy in smaller structures. The size of the possible resolved structures depends on the observed pixel sized and, therefore, on the used lens and the shooting distance. Such areal measures represent a fast and effective way to estimate the heat flux in volcanic areas and can be used to perform quick routine monitoring of both quiescent and active volcanoes.

Experimental data and the results of physical-numerical modeling of the process demonstrate that the heat released by condensation of steam at depth is almost totally transferred by conduction in the uppermost part of the soil (see, e.g., [4]). However, in the areas where the steam does not fully condensate in the soil, the heat transfer mainly occurs by convection of hot fluids emerging as fumaroles. In this last case, pure conductive heat flow cannot be longer assumed because heat is transported to the surface by advective processes [22,55], and the above method cannot be used to estimate the heat flux. Anyway, it is possible to detect zones where heat transport changes from convective to conductive by the change in slope of the thermal gradient [13,42,44].

The proposed method works well for any kind of thermally anomalous areas, both volcanic and hydrothermal, in the condition of a flat emitting surface and in absence of wind, which are very good

approximations for the La Solfatara crater and our measurements. These two parameters have to be taken into account when exporting the recipe outside La Solfatara, modifying the proposed model: this will be the object of future developments of the method.

We have also developed some small utilities, in both FORTRAN and C++, to convert the measured required quantities (surface temperature, air temperature, humidity, background temperature etc.) to total heat released by the soil using the current recipe and, using the CERN ROOT framework, to perform all the required fit and plots. These utilities will be further developed once we have the first drone shoot aerial images to calculate total heat flux over a mapped area. The current versions of such utilities are included in the Supplementary Materials.

6. Conclusions

The estimate of heat release from a large area based on the measurements of the temperature gradient of the ground is very time consuming. Here, we present a method to estimate the heat flux based on the temperature of the surface obtained from an IR camera, together with the measurement of the average air temperature and relative humidity of the area. The method accounts for the heat release by radiation, air convection and water evaporation, and is applied in absence of wind. We applied the method at La Solfatara (Campi Flegrei, Italy). To avoid the effect of sun radiation, measurments were taken at night (between 22:00 and 7:00 local time). For comparison, we also independently estimated the heat flux from measurements of the thermal gradient of the first cm of the ground. Results show a good agreement between the two methods, showing the possibility of using this technique to estimate heat released from large areas. Using thermal cameras carried by flying vectors (drone, helicopter, plane and/or satellite), it is possible to sketch the temperature distribution of thermal anomalies on the ground. Applying our model and method, it will be possible to convert such maps of temperature to maps of heat flux and, by integration, to the total energy released by the soil.

As a future development, we want to perform heat flux measurements using drone-borne thermal cameras and extend the proposed model to include the effects of wind and non-flat topographies.

Supplementary Materials: The following are available online at http://www.mdpi.com/2072-4292/11/2/167/s1, Figure S1: Gradient extrapolation at zero depth vs measured surface temperature for the whole shallow dataset; Figure S2: Plot of the total heat flux from the soil for the whole dataset; FigureS3: Map of the calculated heat flux distribution over the whole investigated area using all points with a direct thermal profile; Figure S4: Separation of the sampled points with $\nabla T_s / q_{soil}$ ratios; Figure S5: Distribution of the five families inside the La Solfatara crater; Tarball S6 (`S6_utils_c++.tar.bz2`): C++ analisys utilities; Tarball S7 (`S7_utils_f90.tar.bz2`) Fortran 90 analisys utilities.

Author Contributions: Conceptualization, E.M., R.P., S.C., G.C. and G.M.; Data curation, E.M., R.P., R.A., P.B., S.C., A.C., G.A. and B.M.; Formal analysis, E.M., R.P., S.C., G.C. and G.M.; Investigation, E.M., R.P., R.A., P.B., S.C., A.C., G.A. and B.M.; Methodology, E.M., R.P., R.A., P.B., S.C., A.C., G.C. and G.M.; Software, R.P., S.C. and G.M.; Supervision, G.C. and G.M.; Validation, E.M., R.P., R.A., S.C., G.C. and G.M.; Visualization, R.P., S.C. and G.M.; and Writing—original draft, E.M., R.P., S.C., G.C. and G.M.

Funding: This research received no external funding.

Acknowledgments: We thank Roberto Isaia for the review of the text and, in particular, of the geological and structural framework of La Solfatara crater.

Conflicts of Interest: The authors declare no conflict of interest.

Abbreviations

The following abbreviations are used in this manuscript:

CL	Confidence Level
DDS	Diffuse Degassing Structure
CFc	Campi Flegrei caldera
IR	Infra Red
sGs	sequential Gaussian simulations
RPAS	Remotely Piloted Aircraft System

References

1. Noguchi, K.; Kamiya, H. Prediction of volcanic eruption by measuring the chemical composition and amounts of gases. *Bull. Volcanol.* **1963**, *26*, 367–378. [CrossRef]
2. Baxter, P.J.; Baubron, J.C.; Coutinho, R. Health hazards and disaster potential of ground gas emissions at Furnas volcano, São Miguel, Azores. *J. Volcanol. Geotherm. Res.* **1999**, *92*, 95–106. [CrossRef]
3. Chiodini, G.; Frondini, F.; Cardellini, C.; Granieri, D.; Marini, L.; Ventura, G. CO_2 degassing and energy release at Solfatara volcano, Campi Flegrei, Italy. *J. Geophys. Res.* **2001**, *106*, 16213–16221. [CrossRef]
4. Chiodini, G.; Granieri, D.; Avino, R.; Caliro, S.; Costa, A.; Werner, C. Carbon dioxide diffuse degassing: Implications on the energetic state of a volcanic hydrothermal systems. *J. Geophys. Res.* **2005**, *110*, B08204. [CrossRef]
5. Frondini, F.; Chiodini, G.; Caliro, S.; Cardellini, C.; Granieri, D.; Ventura, G. Diffuse CO_2 degassing at Vesuvio, Italy. *Bull. Volcanol.* **2004**, *66*, 642–651. [CrossRef]
6. Chiodini, G.; Vilardo, G.; Augusti, V.; Granieri, D.; Caliro, S.; Minopoli, C.; Terranova, C. Thermal monitoring of hydrothermal activity by permanent infrared automatic stations: Results obtained at Solfatara di Pozzuoli, Campi Flegrei (Italy). *J. Geophys. Res.* **2007**, *112*, B12206. [CrossRef]
7. Granieri, D.; Carapezza, M.L.; Chiodini, G.; Avino, R.; Caliro, S.; Ranaldi, M.; Ricci, T.; Tarchini, L. Correlated increase in CO_2 fumarolic content and diffuse emission from La Fossa crater (Vulcano, Italy): Evidence of volcanic unrest or increasing gas release from a stationary deep magma body? *Geophys. Res. Lett.* **2006**, *33*, L13316. [CrossRef]
8. Chiodini, G.; Vandemeulebrouck, J.; Caliro, S.; D'Auria, L.; De Martino, P.; Mangiacapra, A.; Petrillo, Z. Evidence of thermal-driven processes triggering the 2005-2014 unrest at Campi Flegrei caldera. *Earth Planet. Sci. Lett.* **2015**, *414*, 58–67. [CrossRef]
9. Caliro, S.; Chiodini, G.; Paonita, A. Geochemical evidences of magma dynamics at Campi Flegrei (Italy). *Geochim. Cosmochim. Acta* **2014**, *132*, 1–15. [CrossRef]
10. Hochstein, M.P.; Bromley, C.J. Measurement of heat flux from steaming ground. *Geothermics* **2005**, *34*, 133–160. [CrossRef]
11. Friedman, J.D.; Williams, D.L.; Frank, D. Structural and heat flow implications of infrared anomalies at Mt. Hood, Oregon, 1972–1977. *J. Geophys. Res. Solid Earth* **1982**, *87*, 2793–2803. [CrossRef]
12. Frank, D. Hydrothermal Processes at Mount Rainier, Washington. Ph.D. Thesis, Washington University, Seattle, WA, USA, 1985.
13. Aubert, M. Pratical evaluation of steady heat discharge from dormant active volcanoes: Case study of Vulcarolo fissure (Mount Etna, Italy). *J. Volcanol. Geotherm. Res.* **1999**, *92*, 413–429. [CrossRef]
14. Aubert, M.; Diliberto, S.; Finizola, A.; Chébli, Y. Double origin of hydrothermal convective flux variations in the Fossa of Vulcano (Italy). *Bull. Volcanol.* **2008**, *70*, 743–751. [CrossRef]
15. Oppenheimer, C. Infrared surveillance of crater lakes using satellite data. *J. Volcanol. Geotherm. Res.* **1993**, *55*, 117–128. [CrossRef]
16. Wright, R.; Blake, S.; Harris, A.; Rothery, D. A simple explanation for the space-based calculation of lava eruptions rates. *Earth Planet. Sci. Lett.* **2001**, *192*, 223–233. [CrossRef]
17. Sekioka, M.; Yuhara, K. Heat flux estimation in geothermal areas based on the heat balance of the ground surface. *J. Geophys. Res.* **1974**, *79*, 2053–2058. [CrossRef]
18. Yuhara, K.; Sekioka, M.; Ehara, S. Infrared measurement on Satsuma-iwojima Island, Kagoshima, Japan, by helicopter-borne thermocamera. *Arch. Met. Geoph. Biokl. A* **1978**, *27*, 171–181. [CrossRef]
19. Yuhara, K.; Ehara, S.; Tagomori, K. Estimation of heat discharge rates using infrared measurements by a helicopter-borne thermocamera over the geothermal areas of Unzen volcano, Japan. *J. Volcanol. Geotherm. Res.* **1981**, *9*, 99–109. [CrossRef]
20. Stevenson, J.A.; Varley, N. Fumarole monitoring with a handheld infrared camera: Volcán de Colima, Mexico, 2006–2007. *J. Volcanol. Geotherm. Res.* **2008**, *177*, 911–924. [CrossRef]
21. Vilardo, G.; Sansivero, F.; Chiodini, G. Long-term TIR imagery processing for spatiotemporal monitoring of surface thermal features in volcanic environment: A case study in the Campi Flegrei (Southern Italy). *J. Geophys. Res. Solid Earth* **2015**, *120*, 812–826. [CrossRef]

22. Gaudin, D.; Beauducel, F.; Allemand, P.; Delacourt, C.; Finizola, A. Heat flux measurement from thermal infrared imagery in low-flux fumarolic zones: Example of the Ty fault (La Soufrière de Guadeloupe). *J. Volcanol. Geotherm. Res.* **2013**, *267*, 47–56. [CrossRef]
23. Stevenson, D.S. Physical models of fumarolic flow. *J. Volcanol. Geotherm. Res.* **1993**, *57*, 139–156. [CrossRef]
24. Wooster, M.J.; Rothery, D.A. Thermal monitoring of Lascar volcano, Chile, using infrared data from the along track scanning radiometer: A 1992–1995 time series. *Bull. Volcanol.* **1997**, *58*, 566–579. [CrossRef]
25. Harris, A.J.L.; Stevenson, D.S. Thermal observations of degassing open conduits and fumaroles at Stromboli and Vulcano using remotely sensed data. *J. Volcanol. Geotherm. Res.* **1997**, *76*, 175–198. [CrossRef]
26. Kaneko, T.; Wooster, M.J. Landsat infrared analysis of fumarole activity at Unzen volcano: Time series comparison with gas and magma fluxes. *J. Volcanol. Geotherm. Res.* **1999**, *89*, 57–64. [CrossRef]
27. Pieri, D.; Abrams, M. ASTER observations of thermal anomalies preceding the April 2003 eruption of Chikurachki volcano, Kurile Islands, Russia. *Remote Sens. Environ.* **2005**, *99*, 84–94. [CrossRef]
28. Spampinato, L.; Calvari, S.; Oppenheimer, C.; Boschi, E. Volcano surveillance using infrared cameras. *Earth Sci. Rev.* **2011**, *106*, 63–91. [CrossRef]
29. Isaia, R.; Vitale, S.; Di Giuseppe, M.G.; Iannuzzi, E.; D'Assisi Tramparulo, F.; Troiano, A. Stratigraphy, structure, and volcano-tectonic evolution of Solfatara maar-diatreme (Campi Flegrei, Italy). *Geol. Soc. Am. Bull.* **2015**, *127*, 1485–1504. [CrossRef]
30. Cardellini, C.; Chiodini, G.; Frondini, F.; Avino, R.; Bagnato, E.; Caliro, S.; Lelli, M.; Rosiello, A. Monitoring diffuse volcanic degassing during volcanic unrests: The case of Campi Flegrei (Italy). *Sci. Rep.* **2017**, *7*, 6757. [CrossRef]
31. Granieri, D.; Avino, R.; Chiodini, G. Carbon dioxide diffuse emission from the soil: Ten years of observations at Vesuvio and Campi Flegrei (Pozzuoli), and linkages with volcanic activity. *Bull. Volcanol.* **2010**, *72*, 103–118. [CrossRef]
32. Di Vito, M.A.; Isaia, R.; Orsi, G.; Southon, J.; de Vita, S.; D'Antonio, M.; Pappalardo, L.; Piochi, M. Volcanism and deformation since 12,000 years at the Campi Flegrei caldera (Italy). *J. Volcanol. Geotherm. Res.* **1999**, *91*, 221–246. [CrossRef]
33. Orsi, G.; Civetta, L.; Del Gaudio, C.; de Vita, S.; Di Vito, M.A.; Isaia, R.; Petrazzuoli, S.M.; Ricciardi, G.P.; Ricco, C. Short-term ground deformations and seismicity in the resurgent Campi Flegrei caldera Italy: An example of active block-resurgence in a densely populated area. *J. Volcanol. Geotherm. Res.* **1999**, *91*, 415–451. [CrossRef]
34. Petrosino, S.; Damiano, N.; Cusano, P.; Di Vito, M.A.; de Vita, S.; Del Pezzo, E. Subsurface structure of the Solfatara volcano (Campi Flegrei caldera, Italy) as deduced from joint seismic-noise array, volcanological and morphostructural analysis. *Geochem. Geophys. Geosyst.* **2012**, *13*, 1–25. [CrossRef]
35. Bruno, P.P.G.; Ricciardi, G.P.; Petrillo, Z.; Di Fiore, V.; Troiano, A.; Chiodini, G. Geophysical and hydrogeological experiments from a shallow hydrothermal system at Solfatara Volcano, Campi Flegrei, Italy: Response to caldera unrest. *J. Geophys. Res.* **2007**, *112*, B06201. [CrossRef]
36. Byrdina, S.; Vandemeulebrouck, J.; Cardellini, C.; Legaz, A.; Camerlynck, C.; Chiodini, G.; Lebourg, T.; Gresse, M.; Bascou, P.; Motos, G.; et al. Relations between electrical resistivity, carbon dioxide flux, and self-potential in the shallow hydrothermal system of Solfatara (Phlegrean Fields, Italy). *J. Volcanol. Geotherm. Res.* **2014**, *283*, 172–182. [CrossRef]
37. Gresse, M.; Vandemeulebrouck, J.; Byrdina, S.; Chiodini, G.; Revil, A.; Johnson, T.C.; Ricci, T.; Vilardo, G.; Mangiacapra, A.; Lebourg, T.; et al. Three-dimensional electrical resistivity tomography of the Solfatara crater (Italy): Implication for the multiphase flow structure of the shallow hydrothermal system. *J. Geophys. Res. Solid Earth* **2017**, *122*, 8749–8768. [CrossRef]
38. De Siena, L.; Del Pezzo, E.; Bianco, F. Seismic attenuation imaging of Campi Flegrei: Evidence of gas reservoirs, hydrothermal basins, and feeding systems. *J. Geophys. Res.* **2010**, *115*, B09312. [CrossRef]
39. Battaglia, J.; Zollo, A.; Virieux, J.; Dello Iacono, D. Merging active and passive data sets in traveltime tomography: The case study of Campi Flegrei caldera (Southern Italy). *Geophys. Prospect.* **2008**, *56*, 555–573. [CrossRef]
40. Marotta, E.; Calvari, S.; Cristaldi, A.; D'Auria, L.; Di Vito, M.A.; Moretti, R.; Peluso, R.; Spampinato, L.; Boschi, E. Reactivation of Stromboli's summit craters at the end of the 2007 effusive eruption detected by thermal surveys and seismicity. *J. Geophys. Res.* **2015**, *120*, 7376–7395. [CrossRef]

41. Connor, C.B.; Clement, B.M.; XiaoDan, S.; Lane, S.B.; West-Thomas, J. Continuous monitoring of high-temperature fumaroles on an active lava dome, Volcán Colima, Mexico: Evidence of mass flow variation in response to atmospheric forcing. *J. Geophys. Res.* **1993**, *98*, 19713–19722. [CrossRef]
42. Finizola, A.; Ricci, T.; Deiana, R.; Barde Cabusson, S.; Rossi, M.; Praticelli, N.; Giocoli, A.; Romano, G.; Delcher, E.; Suski, B.; et al. Adventive hydrothermal circulation on Stromboli volcano (Aeolian Islands, Italy) revealed by geophysical and geochemical approaches: Implications for general fluid flow models on volcanoes. *J. Volcanol. Geotherm. Res.* **2010**, *196*, 111–119. [CrossRef]
43. Richter, G.; Wassermann, J.; Zimmer, M.; Ohrnberger, M. Correlation of seismic activity and fumarole temperature at the Mt. Merapi volcano (Indonesia) in 2000. *J. Volcanol. Geotherm. Res.* **2004**, *135*, 331–342. [CrossRef]
44. Finizola, A.; Revil, A.; Rizzo, E.; Piscitelli, S.; Ricci, T.; Morin, J.; Angeletti, B.; Mocochain, L.; Sortino, F. Hydrogeological insights at Stromboli volcano (Italy) from geoelectrical, temperature, and CO_2 soil degassing investigations. *Geophys. Res. Lett.* **2006**, *33*, L17304. [CrossRef]
45. Flynn, L.P.; Mouginis-Mark, P.J.; Gradie, J.C.; Lucey, P.G. Radiative temperature measurements at Kupaianaha Lava Lake, Kilauea Volcano, Hawaii. *J. Geophys. Res. Solid Earth* **1993**, *98*, 6461–6476. [CrossRef]
46. Pinkerton, H.; James, M.; Jones, A. Surface temperature measurements of active lava flows on Kilauea volcano, Hawai'i. *J. Volcanol. Geotherm. Res.* **2002**, *113*, 159–176. [CrossRef]
47. Peltier, A.; Finizola, A. Douillet, G.A.; Brothelande, E.; Garaebiti, E. Structure of an active volcano associated with a resurgent block inferred from thermal mapping: The Yasur-Yenkahe volcanic complex (Vanuatu). *J. Volcanol. Geotherm. Res.* **2012**, *243-244*, 59–68. [CrossRef]
48. Al-Arabi, M.; El-Riedy, M.K. Natural convection heat transfer from horizontal plates of different shapes. *Int. J. Heat Mass Trans.* **1976**, *19*, 1399–1404. [CrossRef]
49. Incropera, F.P.; DeWitt, D.P. *Fundamentals of Heat and Mass Transfer*, 4th ed.; John Wiley & Sons Ltd.: Hoboken, NJ, USA, 1996.
50. Jacobson, M.Z. *Fundamentals of Atmospheric Modelling*, 2nd ed.; Cambridge University Press: New York, NY, USA, 2005.
51. Cardellini, C.; Chiodini, G.; Frondini, F. Application of stochastic simulation to CO_2 flux from soil: Mapping and quantification of gas release. *J. Geophys. Res.* **2003**, *108*, 2425–2438. [CrossRef]
52. Deutsch, C.V.; Journel, A.G. *GSLIB Geostatistical Software Library and User's Guide*, 2nd ed.; Oxford Univerity Press: Oxford, UK, 1998; Volume 136.
53. Sawyer, G.M.; Burton, M.R. Effects of a volcanic plume on thermal imaging data. *Geophys. Res. Lett.* **2006**, *33*. [CrossRef]
54. Ball, M.; Pinkerton, H. Factors affecting the accuracy of thermal imageing cameras in volcanology. *J. Geophys. Res.* **2006**, *111*. [CrossRef]
55. Todesco, M.; Chiodini, G.; Macedonio, G. Monitoring and modeling hydrothermal fluid emission at La Solfatara (Phlegrean Fields, Italy). An interdisciplinary approach to the study of diffuse degassing. *J. Volcanol. Geotherm. Res.* **2003**, *125*, 57–79. [CrossRef]